Biochemical and Structural Characterization of *Pseudomonas aeruginosa* Bfd and FPR: Ferredoxin $NADP^+$ Reductase and Not Ferredoxin Is the Redox Partner of Heme Oxygenase under Iron-Starvation Conditions[†,‡]

An Wang,[§] Yuhong Zeng,[§] Huijong Han,[||] Saroja Weeratunga,[§] Bailey N. Morgan,[§] Pierre Moënne-Loccoz,[⊥] Ernst Schönbrunn,[||] and Mario Rivera*[,§]

Ralph N. Adams Institute for Bioanalytical Chemistry and Department of Chemistry, University of Kansas, Multidisciplinary Research Building, 2030 Becker Drive, Room 220 E, Lawrence, Kansas 66047, Department of Medicinal Chemistry, 1251 Wescoe Hall Drive, University of Kansas, Lawrence, Kansas 66045, and Department of Environmental and Biomolecular Systems, OGI School of Science and Engineering at Oregon Health and Science University, Beaverton, Oregon 97006-8921

Received July 3, 2007; Revised Manuscript Received August 24, 2007

ABSTRACT: Among the 118 genes upregulated by *Pseudomonas aeruginosa* in response to iron starvation [Ochsner, U. A., Wilderman, P. J., Vasil, A. I., and Vasil, M. L. (2002) *Mol. Microbiol. 45*, 1277−1287], we focused on the products of the two genes encoding electron transfer proteins, as a means of identifying the redox partners of the heme oxygenase (*pa*-HO) expressed under low-iron stress conditions. Biochemical and spectroscopic investigations demonstrated that the *bfd* gene encodes a 73-amino acid protein (*pa*-Bfd) that incorporates a $[2Fe\text{-}2S]^{2+/+}$ center, whereas the *fpr* gene encodes a 258-residue NADPH-dependent ferredoxin reductase (*pa*-FPR) that utilizes FAD as a cofactor. In vitro reconstitution of *pa*-HO catalytic activity with the newly characterized proteins led to the surprising observation that *pa*-FPR efficiently supports the catalytic cycle of *pa*-HO, without the need of a ferredoxin. In comparison, electron transfer from *pa*-Bfd to *pa*-HO is sluggish, which strongly argues against the possibility that the seven electrons needed by *pa*-HO to degrade biliverdin are transferred from NADPH to *pa*-HO in a ferredoxin (*Bfd*)-dependent manner. Given that *pa*-HO functions to release iron from exogenous heme acquired under iron-starvation conditions, the use of a flavoenzyme rather than an iron−sulfur center-containing protein to support heme degradation is an efficient use of resources in the cell. The crystal structure of *pa*-FPR (1.6 Å resolution) showed that its fold is comparable that of the superfamily of ferredoxin reductases and most similar to the structure of *Azotobacter vinelandii* FPR and *Escherichia coli* flavodoxin reductase. The latter two enzymes interact with distinct redox partners, a ferredoxin and a flavodoxin, respectively. Hence, findings reported herein extend the range of redox partners recognized by the fold of *pa*-FPR to include a heme oxygenase (*pa*-HO).

Pathogenic bacteria need iron to colonize (infect) an organism. However, the concentration of free iron in mammals is typically very low ($\sim 10^{-9}$ M) because it is sequestered by iron-binding and iron-containing compounds such as transferrin, lactoferrin, heme, hemoglobin, and ferritin (*1*). In addition, mammals have evolved means of fighting invading pathogens by making iron even less accessible by reducing levels of transferrin and by downregulating the recycling of iron from macrophages (*2*). It has also been shown that lipocalin 2, an iron-binding protein innate to the immune response, sequesters iron from bacterial siderophores in the early stages of bacterial infection (*3*). It is therefore not surprising that pathogens such as *Neisseriae meningitidis*, *Haemophilus influenzae*, *Shigella dysenteriae*, *Vibrio cholerae*, and the opportunistic *Pseudomonas aeruginosa* have evolved sophisticated mechanisms for iron acquisition, including the utilization of heme iron (*4*, *5*). Heme-containing proteins and in particular hemoglobin constitute an important reservoir of iron given that more than two-thirds of the total iron is chelated by heme and that ∼95% of iron-bound heme is in the form of hemoglobin (*6*). Consequently, many pathogenic bacteria have evolved specific heme uptake systems for acquiring heme iron from mammalian hosts. Although these systems are best understood in Gram-negative bacteria (*4*, *5*), it has been recently shown that *Staphylococcus aureus* not only uses heme as an iron source but also prefers heme iron in the initial stages of infection (*7*). Heme uptake and utilization is also a mechanism used by the

[†] This work was supported by grants from the National Institutes of Health (GM-50503, M.R.) and the National Science Foundation (MCB-0446326, M.R.) and by the Center for Environmental Beneficial Catalysis, University of Kansas, under National Science Foundation Grant (EEC-0310689).

[‡] Coordinates for the structure of *pa*-FPR have been deposited in the Protein Data Bank as entry 2QDX.

* To whom correspondence should be addressed: Ralph N. Adams Institute for Bioanalytical Chemistry and Department of Chemistry, University of Kansas, Multidisciplinary Research Building, 2030 Becker Dr., Room 220 E, Lawrence, KS 66047. Phone: (785) 864-4936. Fax: (785) 864-5396. E-mail: mrivera@ku.edu.

[§] Ralph N. Adams Institute for Bioanalytical Chemistry & Department of Chemistry, University of Kansas.

[||] Department of Medicinal Chemistry, University of Kansas.

[⊥] OGI School of Science and Engineering at Oregon Health and Science University.

10.1021/bi7013135 CCC: $37.00
Published on Web 10/04/2007

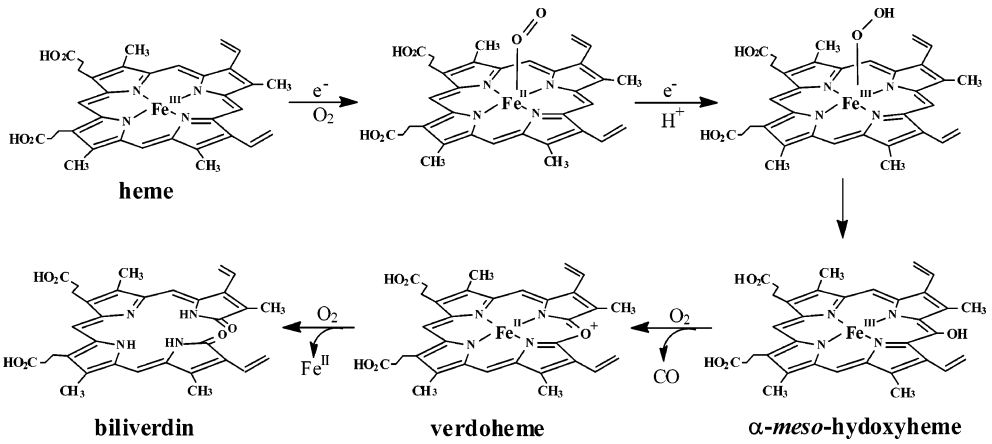

FIGURE 1: Schematic representation of the heme oxygenase catalytic cycle. Emphasis has been placed on the input of the first two electrons that are utilized by the enzyme to reduce coordinated O_2 at the active site. The resultant ferric hydroperoxide intermediate ($Fe^{III}-OOH$) reacts with the macrocycle to form meso-hydroxyheme, which in the presence of O_2 and five additional reducing equivalents is converted to biliverdin and free iron.

opportunistic pathogen *P. aeruginosa*, which can deploy two operons regulated by Fur, the master Fe uptake regulator (*8*). The global iron response associated with Fur-regulated genes includes the heme uptake systems *phu* (*Pseudomonas* heme uptake) and *has* (heme acquisition system). The *phu* locus consists of a receptor gene (*phuR*) and the *phuSTUVW* operon encoding a typical ABC transporter. The second uptake system, *has*, consists of a heme receptor (*hasR*) and a protein that binds heme with high affinity, also known as a hemophore (*4*). Once internalized to the cytoplasm, heme is delivered to a heme oxygenase (*pa*-HO)[1] for its degradation to biliverdin, thus facilitating release of the heme iron for subsequent metabolic use (*9*).

Release of heme iron is accomplished by the breakdown of heme to biliverdin. This is a complex reaction requiring the input of seven electrons and three molecules of O_2, which must be delivered to HO rapidly and efficiently to sustain catalytic activity (Figure 1). Heme breakdown starts with the one-electron reduction of ferric HO (resting state) to the deoxyferrous state, followed by the rapid binding of dioxygen to form an oxyferrous complex ($Fe^{II}-O_2$) (*10*). Injection of a second electron into the $Fe^{II}-O_2$ complex triggers electron rearrangement that leads to the formation of a ferric peroxide ($Fe^{III}-OO^-$) complex, which accepts a proton to form a ferric hydroperoxide ($Fe^{III}-OOH$) oxidizing species (*11*). Ring oxidation involves attack of the $Fe^{III}-OOH$ intermediate on the aromatic macrocycle (*12*) which forms a meso-hydroxyheme intermediate, which undergoes a subsequent O_2- and electron-dependent elimination of the hydroxylated meso carbon as CO, thus forming verdoheme. Verdoheme is then oxidized to the $Fe^{III}-$biliverdin complex in a reaction that requires both O_2 and additional electrons (*13*, *14*). The $Fe^{III}-$biliverdin complex must be reduced to the $Fe^{II}-$biliverdin complex prior to the sequential release of Fe^{II} and biliverdin (*15*).

The identification and characterization of redox partners that deliver electrons to HO, as well as the characterization of protein−protein interactions that facilitate the vectorial electron flow from NAD(P)H to HO, are important steps toward a molecular-level understanding of heme metabolism. Cytochrome P450 reductase supports the catalytic activity of mammalian HO-1 and HO-2 by donating all seven electrons (*15*). In comparison, our current understanding regarding the nature of the redox partner(s) that supports the catalytic activity of bacterial HO enzymes is significantly less developed. It is thought that cyanobacterial and eubacterial HOs are ferredoxin-dependent. It is noteworthy, however, that reports proposing this idea also state that HO activity in cell extracts containing reduced ferredoxin also requires the presence of a second (auxiliary) reductant, such as trolox or ascorbate (*16*−*19*). In fact, in the absence of such auxiliary reducing agents, HO activity is very slow (*16*, *18*) or is arrested at the oxyferrous heme stage (*17*). It is also important to note that despite the widespread belief that bacterial HOs are ferredoxin-dependent the specific ferredoxins that support the activity of these HO enzymes are not yet known. We have recently observed a potentially important clue regarding the nature of the enzymes that transfer electrons to *pa*-HO under conditions of iron starvation. This indication comes from the analysis of relatively recently published data on genes affected by the iron-starvation response in *P. aeruginosa* (*20*), which revealed that the level of expression of 118 genes was increased at least 3-fold under iron-starvation conditions relative to iron-replete conditions. We noticed that among the 118 upregulated genes, the level of expression of a gene encoding a ferredoxin (*bfd*) is increased 203-fold and that of a gene encoding a ferredoxin reductase (*fpr*) 3-fold. These observations suggested to us that the ferredoxin encoded by the *bfd* gene may be the physiological reductant of *pa*-HO, a hypothesis that is in agreement with the fact that among the 118 genes upregulated by iron limitation, the level of expression of the gene encoding *pa*-HO (*pigA*, or PA0672) is also increased 138-fold and that there is no other upregulated gene encoding a ferredoxin or other classical electron transfer protein. Moreover, the product of the *fpr* gene, a ferredoxin reductase (*pa*-FPR), is likely the enzyme that transfers electrons to *pa*-Bfd from NAD(P)H. Hence, the motivation for these studies was to probe a hypothesis

[1] Abbreviations: *Av*-FPR, *Azotobacter vinelandii* ferredoxin reductase; *bfd*, bacterioferritin-associated ferredoxin; *bfr*, bacterioferritin; *Cp*-Fd, *Clostridium pasteurianum* ferredoxin; DTT, dithiothreitol; *Ec*FldR, *Escherichia coli* flavodoxin reductase; EPR, electron paramagnetic resonance; FAD, flavin adenine dinucleotide; NAD(P)H, nicotinamide adenine dinucleotide (phosphate); FNR, ferredoxin NAD(P)H reductase; HO, heme oxygenase; IPTG, isopropyl 1-thiol-D-galactopyranoside; MS, mass spectrometry; *pa*-FPR, *Pseudomonas aeruginosa* ferredoxin reductase; *pa*-HO, *P. aeruginosa* heme oxygenase; PMSF, phenylmethanesulfonyl fluoride.

that the seven electrons needed by *pa*-HO to degrade heme and release iron in the cytosol of *P. aeruginosa* are shuttled from NAD(P)H to *pa*-FPR and subsequently to *pa*-Bfd, which in turn delivers them to *pa*-HO. These investigations uncovered the surprising finding that *pa*-FPR efficiently sustains the catalytic activity of *pa*-HO in vitro, whereas the ferredoxin (*pa*-Bfd) is extremely inefficient at transferring electrons to the oxygenase. These observations strongly suggest that the flavoenzyme *pa*-FPR is the physiological electron donor to *pa*-HO, a situation that is similar that observed with mammalian HOs, which are reduced by the flavoprotein cytochrome P450 reductase.

EXPERIMENTAL PROCEDURES

Cloning and Expression of pa-Bfd and pa-FPR. The genes encoding *pa*-Bfd (PA3530) and *pa*-FPR (PA3397) were synthesized and subcloned into the pET11a vector (GeneScript Corp., Piscataway, NJ). The genes were engineered with silent mutations introducing codons favored by *Escherichia coli* (*21*) and with *Nde*I and *Bam*HI restriction enzyme sites at the 5′ and 3′ ends, respectively, for subcloning into the pET11a vector (Figures S1 and S2 of the Supporting Information). The pET11a vector harboring the *bfd* gene was then transformed into *E. coli* BL21(DE3) Gold cells (Stratagene) for protein expression, whereas that containing the *fpr* gene was transformed into *E. coli* ArcticExpress RIL Competent Cells (Stratagene), to overcome protein misfolding and insolubility issues observed with BL21(DE3) Gold cells. To express *pa*-Bfd, a single colony of *E. coli* BL21(DE3) Gold cells was cultured overnight in 5 mL of LB medium containing 100 μg/mL ampicillin; the cells were subsequently subcultured in 1 L of fresh LB/ampicillin medium and grown at 37 °C until the OD at 600 nm reached 0.5−0.6. Protein expression was then induced by addition of isopropyl 1-thiol-D-galactopyranose (IPTG) to a final concentration of 1 mM, and the cells were cultured for an additional 5 h at 30 °C, before they were harvested by centrifugation (4000 rpm for 10 min) and stored at −20 °C. To express *pa*-FPR, a single colony of ArcticExpress RIL cells was introduced into 10 mL of LB medium containing ampicillin as described above and cultured at 37 °C and 220 rpm overnight. The cell suspension was transferred into 1 L of LB/ampicillin medium and further cultured at 37 °C (4−5 h) to an OD of approximately 0.7. At this point, the cells were transferred to another shaker incubator (Barnstead) pre-equilibrated at 10 °C and cultured for an additional 30 min. Protein expression was then induced by addition of IPTG to a final concentration of 0.3 mM, and the cells were subsequently cultured for approximately 14 h before they were harvested by centrifugation (4000 rpm for 10 min) and stored at − 20 °C.

Purification and Reconstitution of the Iron−Sulfur Cluster in pa-Bfd. One gram of harvested cells was resuspended in 3 mL of lysis buffer [50 mM Tris-HCl (pH 8.0 and 4 °C), 1 mM EDTA, and 100 mM NaCl]. Lysozyme (0.5 mg/mL), PMSF (0.5 mM), and deoxycholic acid (1.3 mg/mL) were added to the cell suspension, followed by stirring at 4 °C for 20 min. Mg^{2+} (final concentration of 4.2 mM) and DNase I (Sigma-Aldrich, St. Louis, MO) were added to the lysate before it was incubated at 37 °C for 30 min. The cell suspension was further incubated at room temperature with stirring for 60 min, followed by centrifugation for 2 h at 23 500 rpm and 4 °C. The pellet was resuspended in 50 mM potassium phosphate buffer (pH 7.0) containing 6 M urea and stirred at room temperature for 60 min. The suspension was centrifuged at 23 500 rpm for 1.5 h; the supernatant containing denatured *pa*-Bfd was placed on an ice bath and bubbled with argon for ∼30 min, followed by addition of DTT (dithiothreitol) to a final concentration of 100 mM, and bubbled with Ar for an additional 15 min. The solution was then diluted 10 times by transferring it into 50 mM potassium phosphate buffer, previously degassed by being bubbled with Ar for 45 min, via a cannula. This was followed by slow addition of previously degassed solutions of $FeSO_4 \cdot 7H_2O$ and Na_2S (200 mM each) to a final concentration of 1.0 mM and incubation with continuous stirring under an argon atmosphere. The resultant solution was subsequently mixed with a suspension of Q-Sepharose resin under a laboratory atmosphere; the resin was allowed to settle, the supernatant discarded, and the resin washed three times, each with 60 mL of 600 mM NaCl in 50 mM potassium phosphate buffer (pH 7.0). The solutions from each of the three washes were combined and dialyzed against 4 L of 50 mM potassium phosphate buffer (pH 7.0) for 3 h before the mixture was loaded onto a column packed with Q-Sepharose [12 cm × 2.5 cm (inside diameter)] pre-equilibrated with the same buffer used for dialysis. The protein was eluted with 50 mM potassium phosphate buffer (pH 7.0) with a salt gradient from 0 to 300 mM NaCl. Fractions containing *pa*-Bfd were pooled together, concentrated, and loaded onto a Sephadex G-50 column [55 cm × 1.5 cm (inside diameter)], which was eluted with previously degassed 50 mM potassium phosphate (pH 7.0) containing 100 mM NaCl. Fractions with an absorbance ratio (A_{424}/A_{280}) larger than 0.5 were pooled, and the resultant solution was concentrated by ultrafiltration and then degassed with argon before being stored at −80 °C.

Characterization of the Fe−S Cluster in pa-Bfd. The purity of overexpressed *pa*-Bfd was analyzed using SDS−PAGE (18% polyacrylamide) and electrospray ionization mass spectrometry; the latter was performed in the Mass Spectrometry Laboratory at the University of Kansas. Molar extinction coefficients of *pa*-Bfd were determined by amino acid analysis at the Molecular Structure, Sequencing and Synthesis Facility, Michigan State University (East Lansing, MI). The electronic absorption spectra of *pa*-Bfd were recorded in 50 mM potassium phosphate buffer (pH 7.0) using a UV−vis S2000 spectrophotometer (Ocean Optics, Dunedin, FL). The protein concentration for the EPR and resonance Raman experiment was ∼1.3 mM in 50 mM HEPES (pH 7) containing 100 mM NaCl and ∼2 mM DTT. EPR spectra of oxidized and reduced *pa*-Bfd were obtained on a Bruker E500 X-band EPR spectrometer equipped with a superX microwave bridge and a dual-mode cavity with a helium flow cryostat (ESR900, Oxford Instruments, Inc.). The same EPR samples were used for the resonance Raman (RR) characterization using a custom Dewar and cold finger to keep the sample temperature at 100 K. The 488 nm excitation (50 mW) of an Innova 90 argon laser (Coherent, Santa Clara, CA) was focused on the sample with a cylindrical lens. The back-scattered light was collected with a camera lens and focused on the entrance slit of a custom McPherson 2061/207 spectrograph (0.67 m with 2400 groove grating) equipped with a Princeton Instruments liquid N_2-cooled CCD detector (LN-1100PB). A Kaiser Optical

supernotch filter was used to attenuate the Rayleigh scattering. Frequencies were calibrated relative to aspirin and are accurate to ± 1 cm^{-1}.

Purification of pa-FPR. Cells were resuspended in 3 mL of lysis buffer, stirred for 20 min at 4 °C, incubated at 37 °C for 20 min, stirred at ambient temperature for 1 h, and then sonicated at 4 °C. The lysed cells were centrifuged at 35 000 rpm for 2 h to sediment cell debris, and the supernatant was dialyzed against 4 L of 20 mM Tris-HCl (pH 7.5, 4 °C) with at least three buffer changes over a period of approximately 16 h. The resultant solution was applied to a Q-Sepharose Fast Flow column [10 cm × 2.5 cm (inside diameter)] previously equilibrated with 20 mM Tris-HCl (pH 7.5, 4 °C). The column was washed with 3 volumes of 20 mM Tris-HCl (pH 7.5) containing 50 mM NaCl, and the protein eluted in the same buffer with a linear gradient (from 50 to 500 mM) of NaCl. Fractions containing FPR (yellow) were pooled, concentrated, and then loaded onto a Sephadex G-50 column (3.0 cm × 100 cm) pre-equilibrated and eluted with phosphate buffer ($\mu = 0.1$, pH 7.0) at 4 °C. Fractions with an A_{280}/A_{450} absorbance ratio of <8 were pooled, and *pa*-FPR was determined to be homogeneous by SDS−PAGE and mass spectrometry. To improve stability during storage (−80 °C), the solutions were made either 0.3 M in NaCl or 10% in glycerol before they were frozen and stored.

Characterization of pa-FPR. The flavin cofactor was released from *pa*-FPR by addition of trichloroacetic acid, which has been described previously (*22*). Denatured protein was removed by centrifugation and the yellow supernatant analyzed by mass spectrometry (MS/MS), which was performed using a Q-Tof-2 hybrid mass spectrometer (Micromass, Manchester, U.K.) housed in the Protein Mass Spectrometry Laboratory at the University of Kansas. The instrument was operated for maximum sensitivity with all lenses optimized while infusing a sample of lysozyme. The cone voltage was 45 eV, and Ar was admitted to the collision cell. Spectra were acquired at a pusher frequency of 11 364 Hz, covering a mass range from 800 to 3000 amu and accumulating data for 5 s per cycle. Time to mass calibration was made with CsI cluster ions analyzed under the same conditions. Samples (500 μg) were desalted on a short column [3 cm × 1 mm (inside diameter)] of polymeric HPLC resin (Hamilton PRP1, Reno, NV) by loading the protein dissolved in a solution of 1% HOAc and eluting the column directly into the source at 25 μL/min with 95% MeOH and 0.08% formic acid.

Electronic Absorption Spectrophotometry. The extinction coefficient of the flavin in *pa*-FPR was determined spectrophotometrically using a previously established protocol (*23*). Electron transfer reactions from NADPH to *pa*-HO using different redox protein mediators were carried out with *pa*-Bfd, *pa*-FPR, spinach ferredoxin, and spinach ferredoxin reductase (Sigma-Aldrich), using a previously reported method with modifications (*24*). The reactions were carried out either in a glovebox (Coy) under O_2-free conditions or in air, in a 1 cm path length cuvette, and monitored by electronic absorption spectroscopy using diode array Ocean Optics (Dunedin, FL) 2000 spectrophotometers equipped with fiber optics. For each reaction, the cuvette was filled with 2 mL of 25 mM HEPES-KOH (pH 7.5), followed by addition of a few microliters of stock solutions of the enzymes and proteins to be tested. In typical experiments, the final concentration of resting state *pa*-HO was 10 μM and the concentrations of *pa*-Bfd, *pa*-FPR, spinach ferredoxin, and spinach ferredoxin reductase were 10 μM, 8 μM, 5 μM, and 0.05 unit/mL, respectively. Catalase (final concentration of 0.1 mg/mL) was used as a H_2O_2 scavenger. The electron transfer reactions were initiated by the addition of a stock solution of NADPH to give a final concentration of 200 μM. The expression system for *pa*-HO (*9*) was a gift from A. Wilks (University of Maryland, College Park, MD), and the protocols for expression and purification of this enzyme have been reported previously (*25*).

Table 1: Summary of Data Collection and Structure Refinement[a]

	FPr liganded with FAD
space group	$P2_12_12$
unit cell dimensions	$a = 68.7$ Å, $b = 74.9$ Å, $c = 52.8$ Å, $\alpha = \beta = \gamma = 90°$
no. of protein atoms	2071 (average *B*-factor = 11.6 Å^2)
no. of ligands	FAD (53 atoms) (average *B*-factor = 8.1 Å^2)
no. of solvent molecules	385 (average *B*-factor = 25.2 Å^2)
rmsd[b] for bonds (Å)	0.01
rmsd[b] for angles (deg)	1.54
resolution range (Å)	15−1.55 (1.6−1.55)
no. of unique reflections	40269 (3620)
completeness (%)	98.9 (95.6)
$I/\sigma I$	26.4 (9.9)
R_{merge} (%)	3.6 (9.9)
R_{cryst}[c] (%)	15.8
R_{free}[d] (%)	19.0

[a] Values in parentheses refer to the highest-resolution shell. [b] Root-mean-square deviation from ideal values. [c] $R_{cryst} = 100 \times \sum|F_{obs} - F_{model}|/\sum F_{obs}$, where F_{obs} and F_{model} are observed and calculated structure factor amplitudes, respectively. [d] R_{free} is the R_{cryst} calculated for randomly chosen unique reflections, which were excluded from the refinement (1234 for FPr liganded with FAD).

X-ray Crystallography. Crystal growing conditions were identified in the High Throughput Screening Laboratory of the Hauptman Woodward Medical Research Institute (Buffalo, NY) (*26*). X-ray-quality single crystals of *pa*-FPR were grown using the hanging drop vapor diffusion method by mixing 2 μL of *pa*-FPR (18 mg/mL) dissolved in 20 mM Tris (pH 7.6) with 2 μL of a solution consisting of 125 mM sodium cacodylate, 200 mM ammonium sulfate, and 20% (w/v) PEG 8000 acetate (pH 6.5). Diffraction data were recorded at −180 °C using the rotation method on a single flash-frozen crystal [detector, R-axis IV^{++} image plate; X-rays, Cu Kα, focused by mirror optics; generator, Rigaku RU300 (MSC, The Woodlands, TX)]. The cryoprotectant was 20% ethylene glycol. X-ray data were reduced with XDS (*27*); the program package CNS (*28*) was employed for phasing and refinement, and model building was performed with O *(29*). The structure was determined by molecular replacement using the coordinates of ferredoxin oxidoreductase from *Azotobacter vinelandii* (PDB entry 1A8P) as a search model, stripped of solvent molecules and ligands. Refinement was performed using data to the highest resolution with no sigma cutoff applied. Several rounds of minimization, simulated annealing (2500 K starting temperature), and restrained individual *B*-factor refinement were carried out. Data collection and refinement statistics are summarized in Table 1.

RESULTS

Overexpression and Purification of pa-Bfd. The *pa*-Bfd protein formed inclusion bodies during overexpression at all

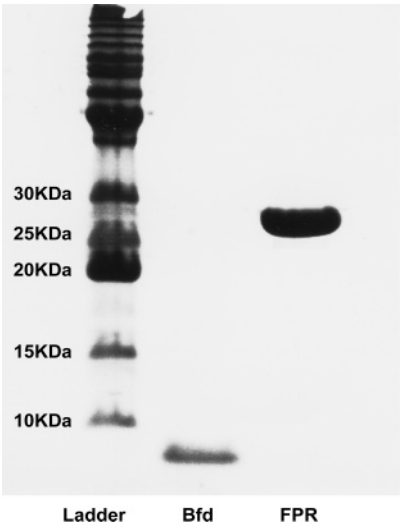

FIGURE 2: SDS−PAGE results obtained from homogeneous solutions of *pa*-Bfd and *pa*-FPR.

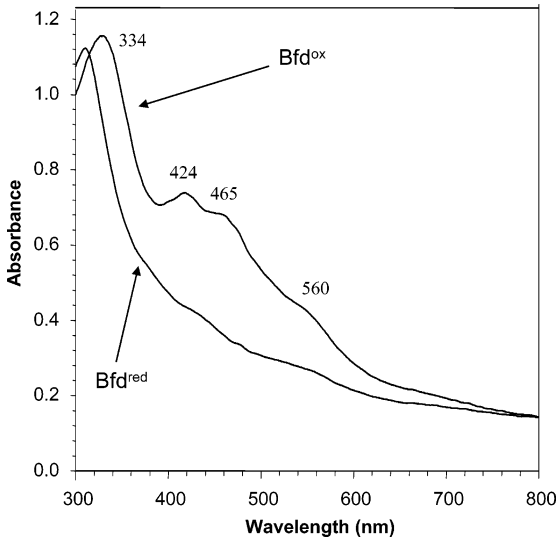

FIGURE 3: Electronic absorption spectra of *pa*-Bfd (25 mM HEPES, pH 7.0) in its oxidized and reduced forms.

three temperatures that were tested (22, 30, and 37 °C). After the cells were lysed, the protein was solubilized from the pellet with the aid of 6 M urea in 50 mM potassium phosphate buffer (pH 7.0). Refolding of *pa*-Bfd and in vitro reconstitution of the Fe−S cluster were carried out anaerobically, on the basis of previously published methods with modifications (*30*−*32*). The rapid decrease in the urea concentration via dilution of the solution 10 times with previously degassed potassium phosphate buffer allows refolding of *pa*-Bfd. In contrast, a slow decrease in the urea concentration via dialysis causes its precipitation, which is likely due to the oxidation of Cys residues. The reconstitution procedure described in Experimental Procedures renders homogeneous *pa*-Bfd (∼2 mg/L), as judged from SDS−PAGE gels (Figure 2). The molecular mass of *pa*-Bfd was determined to be 7823 Da by electrospray ionization mass spectrometry, a value that is in good agreement with the molecular mass calculated from the amino acid sequence, including the initiator methionine (7824 Da).

Spectroscopic Characterization of the Fe−*S Cluster*. The electronic absorption spectrum of oxidized *pa*-Bfd exhibits absorption maxima at 334, 424, 465, and 560 nm (Figure 3). Addition of dithionite produces reduced *pa*-Bfd, which exhibits a nearly featureless electronic absorption spectrum. The electronic absorption spectral features observed with oxidized and reduced *pa*-Bfd are characteristic of ferredoxins containing a $[2Fe\text{-}2S]^{2+/+}$ cluster, such as spinach ferredoxin (*32*), putidaredoxin (*33*), ferredoxin from *Clostridium pasteurianum* (*34*), Bfd isolated from *E. coli* (*35*), and NifU (nitrogen fixation) from the nitrogen-fixing bacterium *A. vinelandii* (*36*). In comparison, $[4Fe\text{-}4S]^{2+/+}$ and $[3Fe\text{-}4S]^{+1/0}$ ferredoxins have a relatively featureless absorption spectrum in the visible region, with only a broad band at ∼400 nm, instead of the two well-defined bands at 424 and 465 nm (*37*, *38*). The molar extinction coefficient (ϵ) of *pa*-Bfd in the visible region was obtained using amino acid analysis. Acid hydrolysis usually causes destruction or modification of Cys, Tyr, Thr, Ser, Met, Asn, and Gln. Hence, only Gly, Ala, Leu, Phe, Lys, Arg, and Pro were used to calculate the concentration of the *pa*-Bfd sample subjected to amino acid analysis. The ϵ values obtained for oxidized *pa*-Bfd at different wavelengths in the visible region are listed in Table 2, where one can see that they are in good agreement with ϵ values of previously characterized $[2Fe\text{-}2S]^{2+/+}$ ferredoxins (*35*, *39*−*41*).

Table 2: Molar Extinction Coefficients of Oxidized *pa*-Bfd and [2Fe-2S] Ferredoxins

	334 nm	424 nm	465 nm	560 nm
ϵ of *pa*-Bfd (mM^{-1} cm^{-1})	11.32	7.33	7.42	3.85
ϵ of typical $[2Fe\text{-}2S]^{2+/+}$ ferredoxin[a] (mM^{-1} cm^{-1})	11−16	6−11	6−10	3−6

[a] Data obtained from ref *36*.

EPR and RR spectroscopic methods were also used to characterize the iron−sulfur cluster in *pa*-Bfd. According to the model proposed by Gibson et al. (*41*), the two iron atoms in a $[2Fe\text{-}2S]^{2+/+}$ cluster interact with one another via the coordinating ligands. Thus, in the oxidized protein, the cluster is EPR silent ($S = 0$) as a consequence of strong antiferromagnetic coupling between the two $S = {}^5/_2$ iron ions. In the reduced protein, the two spins ($S = {}^5/_2$ and $S = 2$) interact antiferromagnetically to give an $S = {}^1/_2$ spin. In agreement, the X-band EPR spectrum of oxidized *pa*-Bfd, in parallel and perpendicular modes, is silent. In comparison, reduced *pa*-Bfd displays a slow relaxing, nearly axial EPR spectrum with a g_{avg} of 1.96 ($g = 2.02$, 1.93, and 1.92) (Figure 4A) diagnostic of the presence of a $[2Fe\text{-}2S]^{+}$ cluster. The *g* values of reduced *pa*-Bfd are identical to those reported for NifU from *A. vinelandii* ($g = 2.02$, 1.93, and 1.91, respectively) (*36*) and very similar to values observed with other $[2Fe\text{-}2S]^{+}$ ferredoxins, such as Bfd from *E. coli* (*35*, *40*), beef adrenodoxin (*42*), putidaredoxin (*43*), and the $[2Fe\text{-}2S]^{+}$ ferredoxin from *C. pasteurianum* (*34*).

The RR spectrum of oxidized *pa*-Bfd obtained with an excitation wavelength of 488 nm is shown in Figure 4B. The three bands at 288, 339, and 391 cm^{-1} are characteristic of $[2Fe\text{-}2S]^{2+}$ ferredoxins (*44*). It is important to note that the spectrum displays a relatively strong band at 288 cm^{-1}, which is diagnostic of ferredoxins harboring a $[2Fe\text{-}2S]^{2+}$ cluster, but it is absent in ferredoxins containing [3Fe-3S] or [4Fe-4S] clusters (*45*−*47*). In addition, the assignments of vibrational frequencies in the RR spectrum of *pa*-Bfd (Table 3) compare very well with vibrational frequencies from

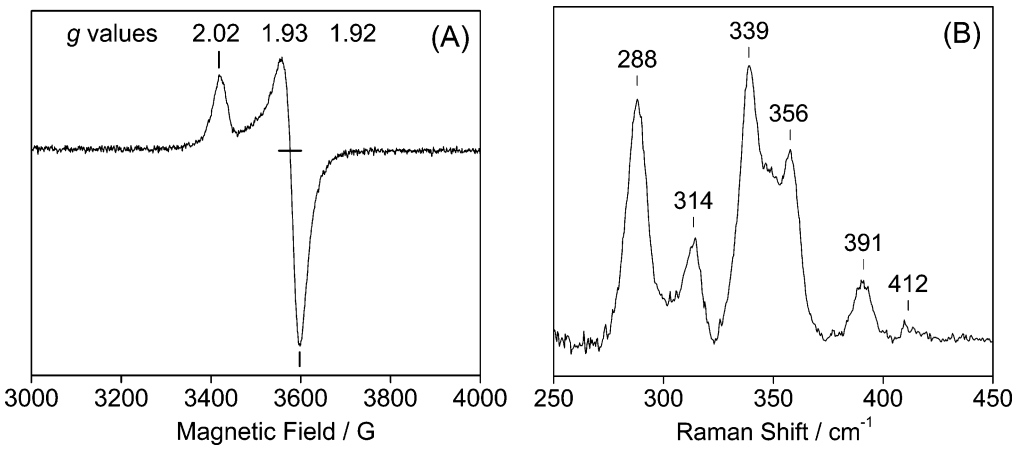

FIGURE 4: (A) X-Band EPR spectrum of dithionite-reduced *pa*-Bfd recorded at 10 K with a microwave power of 0.1 mW, a microwave frequency of 9.66 GHz, and a modulation amplitude of 4 G. (B) Resonance Raman spectra of oxidized *pa*-Bfd in 50 mM potassium phosphate buffer (pH 7.0) containing 100 mM NaCl.

Table 3: Vibrational Assignments from the RR Spectrum of Oxidized *pa*-Bfd

	$B_{2u}{}^b$	$A_g{}^b$	$A_{3u}{}^b$	$B_{1u}{}^t$, $B_{2g}{}^t$	$A_g{}^t$	$B_{1g}{}^b$	$B_{3u}{}^t$	ref
pa-Bfd	412	391	356	−	339	314	288	this study
Av-NifU	417	393	356	−	340	314	288	*36*
bovine adrenodoxin	421	393	349	341	329	317	291	*48*
Cp Fd[a]	404	387	366	353	335	313	290	*48*
So Fd[b]	427	395	367	357	338	329	283	*48*

[a] *Cp* Fd, *C. pasteurianum* ferredoxin. [b] *So* Fd, *Spinacea oleacia* ferredoxin.

previously characterized $[2Fe\text{-}2S]^{2+}$ ferredoxins (*48*−*50*) and synthetic analogue complexes (*51*). In fact, as observed in the EPR spectroscopic studies, the RR spectral features of oxidized *pa*-Bfd are nearly identical to those exhibited by the $[2Fe\text{-}2S]^{2+}$ cluster in the second domain of NifU from *A. vinelandii* (*35*). Taken together, the observations made with electronic absorption, EPR, and RR spectroscopic methods indicate that *pa*-Bfd harbors a $[2Fe\text{-}2S]^{2+/+}$ cluster.

Expression and Characterization of pa-FPR. The *pa*-FPR enzyme was purified to homogeneity, as judged by the presence of a single band in SDS−PAGE gels (Figure 2). The molecular mass of *pa*-FPR measured by ESI-MS is 29 386 Da, a value that is in good agreement with the molecular mass of the enzyme calculated from the sequence, not including the initiator methionine (29387 Da). Solutions containing *pa*-FPR are yellow, which is consistent with the presence of a flavoprotein. Indeed, the electronic absorption spectrum of oxidized *pa*-FPR (Figure 5A) is typical of flavin containing proteins, with bands at 370, 450, and 475 nm; these bands lose their intensity and almost disappear when a solution of NADPH is added to a solution of *pa*-FPR under anaerobic conditions, a spectroscopic property typically observed upon reduction of flavin-containing proteins (*23*).

The nature of the cofactor in *pa*-FPR (FAD or FMN) was determined to be FAD by mass spectrometry, following its extraction from the enzyme into an aqueous solution. The mass spectrum of the *pa*-FPR cofactor (Figure 5-B) exhibits a parent ion peak (X_0) at *m*/*z* 788.41 Da, which corresponds to the calculated mass of FAD + $3H^+$. Fragmentation of this peak in a MS/MS experiment renders peaks at *m*/*z* 439.12, 348.10, and 136.07. The peak at *m*/*z* 439.12 (X_1) corresponds to the FMN + $2H^+$ fragment, the peak at *m*/*z* 348.10 (X_2) to the AMP + H^+ fragment, and the peak at *m*/*z* 136.07 (X_3) to the adenine fragment + $2H^+$. This fragmentation pattern, together with the fact that the mass spectrum of a FAD standard is identical that of Figure 5B, indicates that the cofactor in *pa*-FPR is FAD. The nature of the donor of electrons to FAD, NADH, or NADPH was addressed next. To this end, an anaerobic solution of *pa*-FPR was placed in a cuvette inside a glovebox, where it was mixed with a few microliters of a stock solution of NADPH so that the mole ratio of pyridine nucleotide to enzyme was 10:1, and the reaction was monitored by electronic absorption spectroscopy. The FAD cofactor in *pa*-FPR is reduced rapidly and completely when the enzyme is reacted with NADPH, while in contrast, addition of NADH results in very slow and inefficient reduction. These observations indicate that NADPH is the reducing agent of *pa*-FPR in vivo.

pa-FPR and Not pa-Bfd Is the Donor of Electrons to pa-HO. An important aim of these investigations was to reconstitute and study the catalytic system of heme degradation in vitro using *pa*-FPR, *pa*-Bfd, and *pa*-HO. Initial attempts to reconstitute the catalytic cycle were carried out by adding a few microliters of *pa*-FPR and *pa*-Bfd stock solutions to a solution of *pa*-HO contained in a cuvette under a laboratory atmosphere. Catalase was present in all experiments to scavenge H_2O_2. Heme degradation was subsequently initiated by addition of a few microliters of a stock solution of NADPH and the reaction followed by monitoring changes in the electronic absorption spectrum of *pa*-HO. The Soret band at 405 nm (ferric resting state) shifts to 416 nm with the concomitant appearance and increase in intensity of bands at 542 and 577 nm (Figure 6A), which indicate formation of the oxyferrous complex. Conversion of the latter to the iron−biliverdin complex is manifested in the time-dependent decay of the 542 and 577 nm bands (∼13 min), which results in the featureless visible spectrum characteristic of the iron−biliverdin complex (*52*). Consistent with the formation of the iron−biliverdin complex, addition of acid to the solution in the cuvette causes the release of iron from the iron−biliverdin complex and results in the immediate formation of a band at 685 nm, which is diagnostic of biliverdin. The

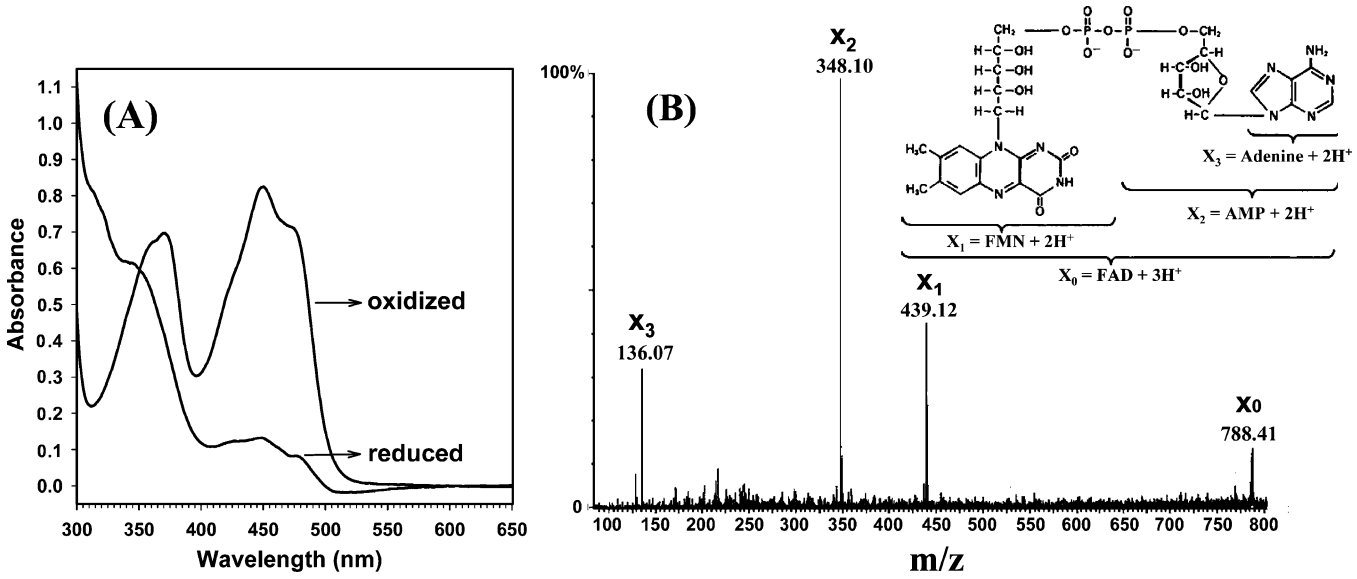

FIGURE 5: (A) Electronic absorption spectra of *pa*-FPR in oxidized and reduced form. (B) MS/MS spectrum of the cofactor extracted from *pa*-FPR. The fragmentation pattern unequivocally identifies the cofactor as FAD.

spectra in Figure 6A also show that transformation of the oxyferrous complex into the iron−biliverdin complex occurs without noticeable accumulation of relatively stable intermediates such as verdoheme, which displays a characteristic band at 660 nm (*53*). Although these results seem to suggest participation of *pa*-Bfd and *pa*-FPR in relaying electrons from NADPH to *pa*-HO, additional experimentation showed that transfer of electrons from *pa*-Bfd to *pa*-HO is a slow process, whereas transfer of electrons from *pa*-FPR to *pa*-HO is fast. In fact, results from these experiments (see below) demonstrate that *pa*-FPR alone supports the efficient degradation of heme to the iron−biliverdin complex in vitro.

The time-dependent change in the intensity of the 542 nm band in the experiment described above was plotted as a function of time [Figure 6B (□)]. The initial rapid increase in intensity demonstrates that in the presence of *pa*-Bfd and *pa*-FPR, delivery of the first electron, followed by the binding of O_2 (see Figure 1), occurs in less than 1 min. The more gradual decay in the intensity of the 542 nm band indicates that degradation of the oxyferrous complex to the iron−biliverdin complex occurs in approximately 13 min. It was therefore striking that in a similar experiment conducted with a solution containing *pa*-FPR and *pa*-HO, but not *pa*-Bfd [Figure 6B (●)], formation of the oxyferrous complex and subsequent degradation to the iron−biliverdin complex occurred at rates almost identical to those observed for the system with all three proteins, *pa*-HO, *pa*-Bfd, and *pa*-FPR, thus suggesting that *pa*-FPR alone supports the catalytic activity of *pa*-HO. The profile of heme degradation shown by the circles in Figure 6B was obtained with equimolar concentrations (8 μM) of *pa*-HO and *pa*-FPR. Thus, the dependency of *pa*-FPR concentration on heme degradation was explored by lowering the concentrations of *pa*-FPR to 3.2, 0.8, and 0.08 μM, while maintaining the concentration of *pa*-HO at 8 μM. Results from these experiments (Figure 6C) showed that when the concentration of *pa*-FPR is 3.2 (▲) or 0.8 μM (○), the same trend as that represented by the circles in Figure 6B is observed, that is, relatively fast formation of the oxyferrous complex followed by its slower conversion to the iron−biliverdin complex. As indicated above, formation of biliverdin is corroborated by addition of acid, which results in the immediate formation of a band at 685 nm. When *pa*-FPR is present at 0.08 μM, the reaction profile [Figure 6C (■)] shows the formation of a steady state concentration of the oxyferrous complex in the time period that was investigated. Nevertheless, addition of acid to the cuvette after 1800 s results in the immediate formation of a band at 685 nm, which indicates that oxidation of heme to the iron−biliverdin complex, although incomplete, still occurs when the ratio of *pa*-HO to *pa*-FPR is 100.

The notion that *pa*-Bfd is not required to support the catalytic activity of *pa*-HO was further tested by studying the electron transfer reaction from reduced *pa*-Bfd or reduced *pa*-FPR to resting state *pa*-HO. To this end, a stock solution of reduced *pa*-FPR was prepared in a glovebox by addition of 1 equiv of NADPH to a solution of oxidized *pa*-FPR. This resulted in complete reduction of oxidized *pa*-FPR, as judged by the disappearance of the yellow color and by the electronic absorption spectrum of the resultant solution. A few microliters of the solution containing reduced *pa*-FPR (1 equiv) was added to a solution of resting state *pa*-HO contained in a cuvette. The reaction was monitored by the appearance and growth of bands at 430 and 560 nm (Figure 6D), which are characteristic of deoxyferrous *pa*-HO; these spectral changes display clear isosbestic points, indicating that the process involves only the one-electron reduction of resting state *pa*-HO. The time-dependent increase in the intensity of the 430 nm band, plotted with filled circles in the inset of Figure 6C, shows that the reduction of resting state *pa*-HO by reduced *pa*-FPR occurs rapidly and efficiently. If a similar experiment is performed with excess NADPH, to mimic the conditions of the heme oxygenase assays described above, the reduction of resting state *pa*-HO is complete in less than 1 min (data not shown). This observation is consistent with the rapid formation of the oxyferrous complex of *pa*-HO when NADPH is present in excess (see Figure 6B). In this context, it is important to note that NADPH alone does not reduce *pa*-HO, which is apparent from the negligible changes in absorbance at 430 nm upon addition of excess NADPH to resting state *pa*-HO under anaerobic conditions (triangles in the inset of Figure 6D). Experiments conducted by adding 1 equiv of reduced

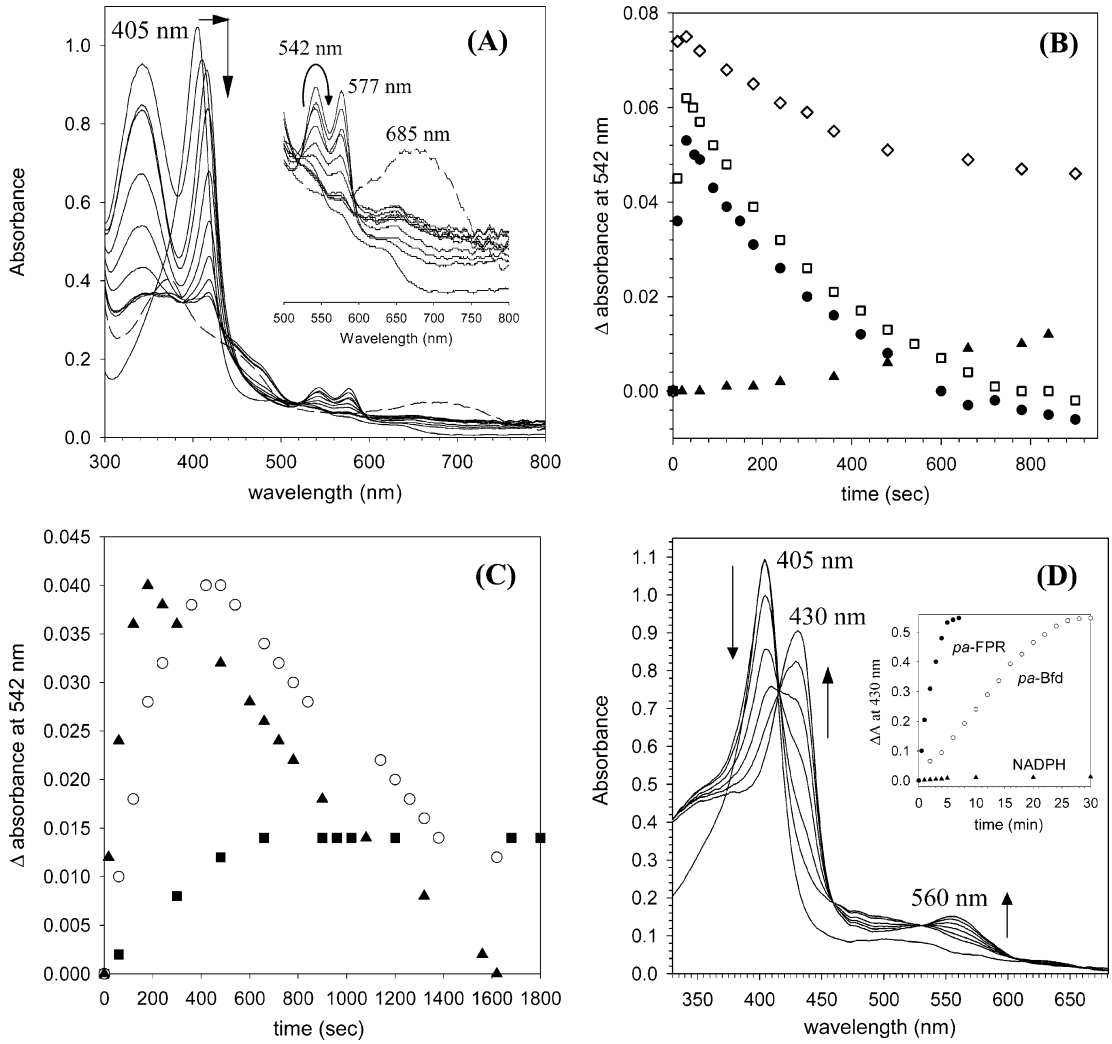

FIGURE 6: (A) Spectral changes that take place upon addition of NADPH (200 μM) to a solution containing *pa*-HO (8 μM), *pa*-FPR (8 μM), and *pa*-Bfd (10 μM). The inset shows the time-dependent growth and subsequent decrease of the intensity of the 542 and 577 nm bands, which is a manifestation of accumulation of the oxyferrous complex and its subsequent conversion to iron biliverdin. The band at 685 nm is formed instantaneously upon addition of acid to the iron−biliverdin complex. (B) Time-dependent plot of the formation of the oxyferrous complex (542 nm) in panel A and its subsequent decay to the iron−biliverdin complex for systems containing *pa*-HO and *pa*-FPR (●), *pa*-HO, *pa*-Bfd, and *pa*-FPR (□), *pa*-HO and FNR (▲), and *pa*-HO, Fd, and FNR (◇). (C) Time-dependent plot of the formation of the oxyferrous complex (542 nm) and its decay to the iron−biliverdin complex for systems containing a constant concentration of *pa*-HO (8 μM) and 3.2 μM *pa*-FPR (▲), 0.8 μM *pa*-FPR (○), and 0.08 μM *pa*-FPR (■). The reaction was initiated by addition of NADPH (200 μM). (D) Spectral changes taking place upon addition of reduced *pa*-FPR (8 μM) to resting state *pa*-HO (8 μM) under anaerobic conditions. The appearance and growth of a band at 430 nm are diagnostic of the formation and accumulation of deoxyferrous *pa*-HO. The inset shows a time-dependent plot of the formation of deoxyferrous *pa*-HO (430 nm) upon addition of reduced *pa*-FPR (●) and upon addition of reduced pa-Bfd (○) to resting state *pa*-HO. All experiments were carried out at 25 °C in the presence of catalase. Concentrations in parentheses correspond to solutions in the cuvette (final concentration).

pa-Bfd to resting state *pa*-HO (empty circles in the inset of Figure 6D) reveal that the reduction of resting state *pa*-HO by *pa*-Bfd is slow compared to the reduction of resting state *pa*-HO by *pa*-FPR. Hence, these observations are in good agreement with those described above indicating that the rate of heme degradation in the presence of *pa*-FPR is unaltered by the addition of *pa*-Bfd. Taken together, these findings suggest that *pa*-FPR is the redox partner of *pa*-HO in vivo.

Given that the heme degradation carried out by *pa*-HO is supported by *pa*-FPR alone, we probed whether another flavoenzyme, spinach ferredoxin $NADP^+$ reductase (FNR), would also support the catalytic activity of *pa*-HO. We found that addition of excess NADPH to a solution containing an equimolar mixture of resting state *pa*-HO and FNR does not appreciably reduce resting state *pa*-HO. This is clearly manifested in the nearly negligible changes in the intensity of the 542 nm band diagnostic of oxyferrous complex formation (triangles in Figure 6B). The fact that FNR cannot reduce *pa*-HO suggests that the efficient redox reaction between *pa*-FPR and *pa*-HO is a consequence of specific interactions among these two enzymes. It is also interesting that when the activity of *pa*-HO is reconstituted with FNR and spinach ferredoxin, the addition of NADPH causes rapid spectral changes diagnostic of the formation of the oxyferrous complex; i.e., the Soret band shifts to 416 nm with the simultaneous appearance and growth of bands at 542 and 577 nm. Plotting the intensity of the band at 542 nm as a function of time (diamonds in Figure 6B) underscores the rapid formation of the oxyferrous complex and reveals that its conversion to the iron−biliverdin complex is slow. Formation of the latter was corroborated by the sudden appearance of the 685 nm band, diagnostic of biliverdin, upon

acidification of the solution in the cuvette. These observations indicate that spinach ferredoxin can efficiently transfer one electron to resting state *pa*-HO, which upon one-electron reduction binds O_2 to form the oxyferrous complex. The very slow decay of the band at 542 nm, however, indicates that transfer of a second electron to $Fe^{II}-O_2$, which is necessary to trigger the electronic rearrangement leading to the formation of the $Fe^{III}-OOH$ oxidizing species, is inefficient, even if there is excess NADPH and thus reduced ferredoxin. Consequently, although spinach ferredoxin can act as an efficient one-electron reductant, it cannot deliver the second electron efficiently, which is a key step in the mechanism of O_2 activation that leads to heme degradation. This situation is reminiscent of that observed with cytochrome $P450_{cam}$ (from *Pseudomonas putida*), which is reduced from the ferric to the ferrous oxidation state by several ferredoxins, including that from spinach. However, reduction of the corresponding $Fe^{II}-O_2$ complex, which triggers the electronic rearrangement necessary to form the obligatory $Fe^{III}-OOH$ intermediate, is attained only in the presence of the physiological reductant putidaredoxin (*54*).

The idea that the degradation of heme by *pa*-HO and presumably by HOs in other pathogenic organisms does not require an iron−sulfur cluster protein is not only novel but also consistent with the fact that the genes encoding these enzymes are upregulated by iron starvation (*20*). Hence, in the sense of efficient iron utilization, it does not seem economical for the cell to assemble iron−sulfur cluster proteins for the purpose of acquiring iron. Instead, utilization of a flavoprotein to deliver the seven electrons needed to break down heme sequestered from the host obviates the need to further deplete the already scarce iron reserves in order to acquire additional supplies of this nutrient. In this context, it is also important to underscore that mammalian HOs (HO-1 and HO-2) are reduced by a flavoprotein, cytochrome P450 reductase, and not by a small electron transfer protein (*52*, *55*−*57*).

Structure of pa-FPR. The polypeptide in *pa*-FPR folds into the classical two-domain structure of ferredoxin NAD(P)H reductases (Figure 7A), which includes spinach FNR. The N-terminal domain, residues 1−87, comprises an antiparallel β-barrel (β1−β6) capped by helix α1, where FAD binds near the N-terminal end of α1 and the carboxy ends of β4 and β5. The C-terminal domain, residues 104−258, folds into the typical nucleotide binding fold comprised of a five-stranded parallel β-sheet (order β9, β8, β7, β10, β11) that is surrounded by nine α-helices (α2−α10). The $NADP^+$ domain in ferredoxin reductases of known structures is across the carboxy-terminal domain of the β-sheet encompassing β7, β10, the loop connecting β7 to α3, and the N-terminal residues of α3. The $NADP^+$ and FAD binding domains are joined mainly by α3, α6, and to a certain extent α5 and by the loops preceding and succeeding it. This interface produces a deep cleft where the FAD and $NADP^+$ cofactors reside in the proximity of one another. Finally, the two domains are linked by residues 88−103, which comprise elements of secondary structure (β6, loop, and α2).

The structure of *pa*-FPR is very similar to that characteristic of the superfamily of NAD(P)H reductases and most similar to the structure of NADPH ferredoxin reductase from *A. vinelandii* (*Av*-FPR) (*58*). The latter is perhaps not surprising, given the 85% amino acid identity and 91% similarity between the two enzymes (see Figure 7B). The high degree of structural identity can be seen in the superposition (rmsd for C_α atoms of 0.42 Å) of *pa*-FPR (red) and *Av*-FPR (blue) shown in Figure 7C, in a view identical that in Figure 7A. Only a few amino acids differ in the position of their C_α atoms; these are Ser2, Gly74, Arg186, and Glu257. The position of Ser2 in the amino-terminal sequence is expected to impart it with a large *B*-factor, which is likely the reason for the discrepancy in the C_α position of this residue in the two structures. R186 is located in the middle of the loop connecting β9 with α8; thus, it would also be expected to experience conformational flexibility. This leaves Gly74 and Glu257, which are located in the FAD binding domain, where the largest differences in structure are observed between *pa*- and *Av*-FPR. In both crystal structures, the *B*-factors exhibited by these residues are very close to the average *B*-factor for each structure, which suggests that Gly74 and Glu257 have low conformational flexibility. Consequently, the differences in the crystal structures likely represent subtle differences in the way in which each of the enzymes interacts with their FAD cofactors.

The FAD cofactor binds to *pa*-FPR using contacts that are typical of the superfamily of NAD(P)H reductases; these conserved sequences are highlighted in Figure 7B. Among residues in the R^{51}xYS/T motif in strand β4, the side chain of R51 hydrogen bonds with the phosphate in the FMN moiety, the carbonyl oxygen of A52 accepts a hydrogen bond from the ribityl C2′ hydroxyl, the hydroxyl group in Y53 hydrogen bonds with the ribityl C4′ hydroxyl, and the aromatic side chain in the same residue π-stacks against the isoalloxazine ring (see Figure 8). The phosphate in the FMN portion of the cofactor is stabilized by hydrogen bond interactions with the amides of L76 and T77, which are part of the G^{74}xxT/S motif near the amino-terminal section of helix α1. The FAD cofactor in *pa*-FPR adopts a conformation that places the isoalloxazine and adenine rings close to each other. This conformation is similar that adopted by the FAD cofactor in *Av*-FPR (*58*) and *E. coli* flavodoxin reductase (*Ec*FldR) (*59*) but distinct from that seen in spinach FNR (*60*) and other members of the reductase family (*61*), where an extended cofactor places the adenine ring distant from the isoalloxazine moiety. As in the structures of *Av*-FPR and *Ec*FldR, the adenine ring in the cofactor of *pa*-FPR π-stacks with the aromatic side chain of F255; this residue is F255 in *Av*-FPR and W255 in *Ec*FldR. Hence, the observations made with the crystal structure of *pa*-FPR support the idea that the conformation of FAD in *Av*-FPR, *Ec*FldR, and now *pa*-FPR is driven by stabilizing π-stacking interactions (*58*). In comparison, the adenine ring in spinach FNR is extended into the surface of the protein, where it π-stacks with the side chain of Y120. It is also worth noting that similar to the structure of *Av*-FPR, the structure of *pa*-FPR lacks an aromatic side chain on the face of the isoalloxazine ring, opposite the side that interacts with Y53 of the R^{51}xYS/T motif on β4. Instead, the fold of *Av*-FPR and *pa*-FPR places A254 at the equivalent position, where the side chain of A254 is directed away from the isoalloxazine ring. It has been pointed out in the context of the structure of *Av*-FPR that the carbonyl oxygen of A254 and its negatively charged dipole may alter the electronic structure of the isoalloxazine ring, which may account for the absence of a stable

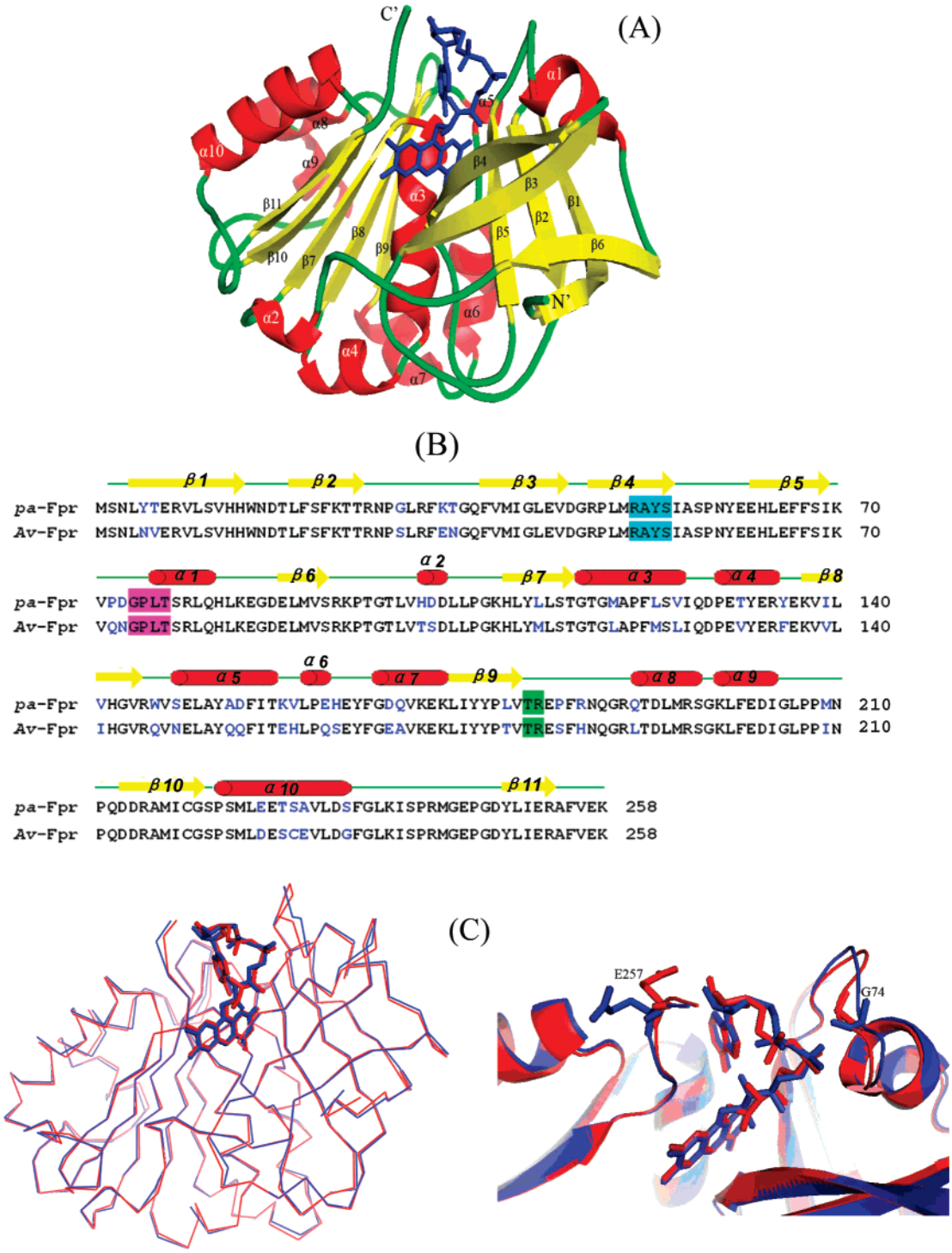

FIGURE 7: (A) View of *pa*-FPR depicting the two domains and the bound FAD. (B) Amino acid sequence alignment of *pa*-FPR and *Av*-FPR using ClustalW. Residues distinct among the two enzymes are colored blue. The conserved sites for binding the isoalloxazine ring of FAD and phosphates P_1 and P_2 are highlighted in cyan, magenta, and green, respectively. (C) Superposition of *Av*-FPR (blue) and *pa*-FPR (red) obtained using the Protein3Dfit server shows a C_α rmsd of 0.416 Å (left). The view is like that in panel A.

semiquinone state in this enzyme (*58*). It is therefore interesting that a stable semiquinone state is also not observed in *pa*-FPR because it suggests that the electronic structure of the isoalloxazine ring in this enzyme is similar to that of *Av*-FPR and distinct from those of other reductases. An additional difference pointed out between *Av*-FPR and other reductases in the superfamily (*58*) is the three-amino acid carboxy-terminal extension, which includes K258 as the terminal residue. The side chain of this residue, together with the side chain of R51 in the R^{51}xYS/T motif, interacts electrostatically with the two phosphate groups of FAD. A similar electrostatic interaction between K258 and one of the phosphate groups in the FAD cofactor is also present in the structure of *pa*-FPR (Figure 8), which also has the three-amino acid carboxy-terminal extension in its sequence. Hence, it appears that the microenvironment of FAD in *pa*-FPR is very similar that of FAD in *Av*-FPR but distinct from that observed in other enzymes from the ferredoxin reductase

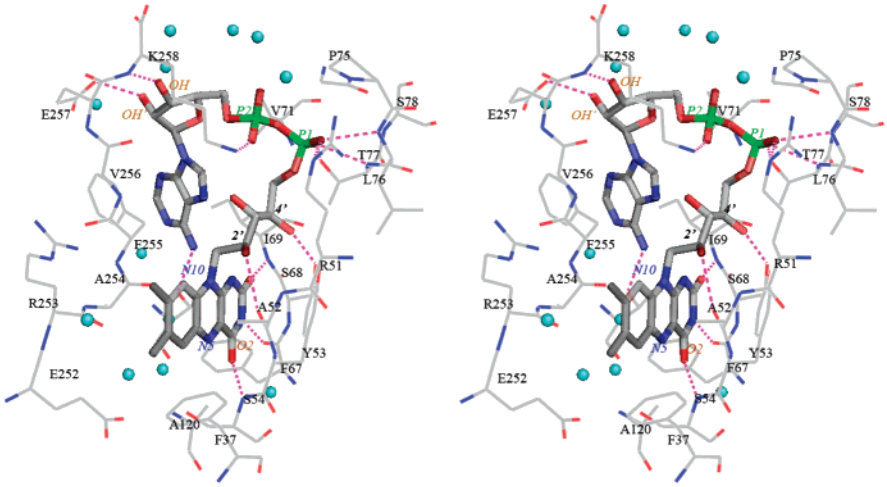

FIGURE 8: Stereoview of the FAD binding site in *pa*-FPR.

family. How these subtle differences affect reactivity and perhaps redox complementarity with physiologic partners remains to be investigated.

DISCUSSION

Pa-FPR Supports the Efficient Degradation of Heme by pa-HO. The work described here was undertaken with the aim of identifying and characterizing the proteins that are involved in delivering the seven electrons required by *pa*-HO to oxidize the heme macrocycle to biliverdin and release its iron. Previous reports suggested that HOs in cyanobacteria and eubacteria are ferredoxin-dependent and thus thought to receive electrons from NAD(P)H via ferredoxin reductase and ferredoxin. It is interesting, however, that the rates of heme degradation observed in the presence of ferredoxin are typically slow, unless a second reducing agent such as ascorbate, isoascorbate, or trolox is added to the system (*16*−*19*). In this context, it should be pointed out that ascorbate or other similar reducing agents cause heme degradation by two chemically distinct processes, heme oxygenation (as seen in the normal catalytic cycle of HO) and coupled oxidation (*62*−*64*). The process of heme oxygenation occurs as outlined in Figure 1, where O_2 coordinated to iron is reduced to HOO^-, to form the ferric hydroperoxide (Fe^{III}−OOH) intermediate within the active site of heme oxygenase; Fe^{III}−OOH adds an OH group to the macrocycle to form meso-hydroxyheme. In contrast, in the coupled oxidation process, noncoordinated O_2 is reduced to H_2O_2 by the reducing agent (i.e., ascorbate) outside the enzyme (*64*). Once formed, H_2O_2 can diffuse into the active site and react with ferrous heme to form meso-hydroxyheme, which is then channeled to the iron−biliverdin complex using additional electrons from ascorbate. Thus, the processes of heme oxygenation and coupled oxidation differ fundamentally in the form in which O_2 is reduced to H_2O_2 (*64*). In addition, it is also important to consider that resting state (ferric) HO can bind exogenous H_2O_2 to form the Fe^{III}−OOH intermediate, which decays into meso-hydroxyheme (*12*, *53*). Because exogenous H_2O_2 is readily formed when dissolved O_2 reacts with electron donors such as NADPH, ascorbate, hydrazine, etc., it is important that assays of HO activity include catalase to destroy exogenous H_2O_2, thus preventing the oxidation of heme by paths other than the catalytic cycle of heme oxygenase. In this context, it is important to note that with only one exception, assays for determining the activity of "ferredoxin-dependent" HOs do not include catalase (*16*−*19*). Interestingly, the study that reports on the inclusion of catalase in the heme degradation assays found that the oxyferrous complex is formed readily; decay of this complex into the iron−biliverdin complex, however, is a very slow process (*17*). In contrast, when ascorbate was added as the auxiliary electron donor in addition to ferredoxin, the oxyferrous complex decayed rapidly to biliverdin, even if catalase was present (*17*). Consequently, it was suggested that in addition to ferredoxin, an auxiliary electron donor is necessary to carry out the catalytic activity of bacterial HOs. It is therefore significant that findings reported here demonstrate that when *pa*-FPR is the redox partner of *pa*-HO the degradation of heme to the iron−biliverdin complex occurs rapidly and efficiently in the absence of an auxiliary electron donor, despite the fact that all assays were carried out in the presence of catalase (Figure 6B,C). It is also significant that concentrations of *pa*-FPR at least 10-fold lower than that of *pa*-HO sustain the efficient degradation of heme by *pa*-HO in vitro. When the concentration of *pa*-FPR is lowered 100-fold relative to that of *pa*-HO, degradation of heme is slower; nevertheless, the iron−biliverdin complex is still formed. The efficiency of *pa*-FPR in supporting the in vitro degradation of heme by *pa*-HO is lower than that with which cytochrome P450 reductase supports the catalytic activity of HO-1 because the latter efficiently degrades heme when the proportion of oxygenase to reductase is 100-fold (*52*, *57*). A plausible reason for the higher efficiency displayed by cytochrome P450 reductase may reside in the fact that this enzyme contains both FAD and FMN as cofactors and that electrons can be delivered to HO-1 by either cofactor in different steps of the catalytic cycle (*52*).

It is also important to note that our attempts to support the catalytic activity of *pa*-HO with another flavoprotein (spinach FNR) did not result in appreciable activity, thus suggesting that *pa*-HO and *pa*-FPR associate specifically to form optimum complexes that facilitate the electron transfer events leading to heme degradation. In addition, when *pa*-HO activity was assayed using spinach ferredoxin as the electron donor (Figure 6B), there was rapid accumulation of the oxyferrous complex; subsequent decay to the iron−biliverdin complex, however, was very slow. This observation, which is reminiscent of that made with ferredoxin-

dependent HOs in the absence of an auxiliary electron donor, supports the notion that *pa*-HO and *pa*-FPR specifically interact in the cytosol of *P. aeruginosa* to release iron from exogenously acquired heme. The study of these interactions will be facilitated by the availability of crystal structures for *pa*-HO (*65*) and *pa*-FPR and by the availability of sequential backbone NMR assignments for *pa*-HO (*66*). This information will make it possible to carry out chemical shift perturbation experiments (*67*) aimed at experimentally defining the interprotein interface once the sequential assignments of *pa*-FPR have been obtained, a task that is currently underway in our laboratories. A final comment regarding heme degradation pertains to the observation that in vitro heme is degraded to the iron−biliverdin complex, not biliverdin; the release of iron requires the addition of acid or a chelating agent such as desferroxiamine. This may reflect the fact that iron in vivo is highly regulated, and therefore, it is likely to be escorted out of the HO−biliverdin complex by a chaperone protein that shuttles it to a place where it will be incorporated into an iron−sulfur or heme cofactor. One other alternative is that a protein other than *pa*-FPR reduces the Fe^{3+} in the iron−biliverdin chelate bound to *pa*-HO and facilitates release of Fe^{2+}. Identification of this putative protein may constitute the next significant advance in piecing together the path that allows *P. aeruginosa* to use heme iron as a nutrient.

The crystal structure of *pa*-FPR revealed a fold typical of the ferredoxin reductase superfamily and provided unequivocal corroboration of biochemical observations described herein, indicating that the flavin cofactor is FAD. Structural comparisons indicate that the structure of *pa*-FPR is almost identical to that of *Av*-FPR and very similar to that of *E. coli* flavodoxin reductase. The function of the latter two enzymes has been proposed to be their participation in a putative redox pathway leading to protection against oxidative stress, which is carried out by performing the reductive repair of O_2^--damaged hydroxylases, such as the [Fe-S] cluster-containing aconitase (*68*, *69*). Additional studies suggest that a function of *Av*-FPR and *Ec*FldR is to maintain tolerable levels of NADPH during oxidative stress, thereby preventing reduction of iron and other transition metals that catalyze the formation of highly toxic hydroxyl radicals via Fenton-type chemistry (*69*). It is therefore remarkable that although the structures of *Av*-FPR and *Ec*FldR are nearly identical, each utilizes a different type of redox partner; *Av*-FPR interacts specifically with FdI, a protein containing [3Fe-4S]$^{+/0}$ and [4Fe-4S]$^{2+/+}$ clusters (*70*), whereas *Ec*FldR interacts with a flavodoxin (*71*). Our findings extend the range of possible redox partners for the same fold (*pa*-FPR) to include a bacterial heme oxygenase (*pa*-HO) which metabolizes heme in the cytosol of *P. aeruginosa*. This notion is supported by the fact that some bacteria and algae possess flavodoxins capable of efficiently replacing ferredoxins as electron transfer proteins and that the expression of these proteins is induced under conditions of iron starvation, which limit the biosynthesis of [Fe−S] clusters and thus the assembly of electron transfer ferredoxins (*61*, *72*).

Bfd May Function as a Scaffold for the Assembly of Iron−Sulfur Clusters. The biochemical and spectroscopic investigations reported above clearly indicate that Bfd harbors a [2Fe-2S]$^{2+/+}$ cluster typical of ferredoxins. Nevertheless, transfer of electrons from *pa*-Bfd to *pa*-HO is sluggish, thus strongly suggesting that these two proteins are not redox partners in vivo. A Blast search using *pa*-Bfd as a query revealed equivalent proteins in several bacteria; members of this family contain four conserved cysteine residues organized in a unique **C**-X-**C**-X_{31-34}-**C**-X_2-**C** arrangement, which are thought to function as ligands in the [2Fe-2S]$^{2+/+}$ cluster. Efforts to structurally characterize *pa*-Bfd are ongoing in our laboratories. The EPR and vibrational features of *pa*-Bfd are identical to those reported for the [2Fe-2S]$^{2+/+}$ cluster in NifU, which is a multidomain protein required for the assembly of the metallo cluster in nitrogenase (*73*). However, unlike members of the NifU family, *pa*-Bfd is a single-domain protein that would seem to be analogous to [2Fe-2S]$^{2+/+}$-containing ferredoxins of bacteria, plants, and algae. The latter, nonetheless, are ∼50 residues longer than Bfds and do not exhibit the unique **C**-X-**C**-X_{31-34}-**C**-X_2-**C** arrangement of Bfds. Consequently, it is tempting to speculate that Bfd does not function as a classical electron transfer ferredoxin but instead serves as a scaffold for [2Fe-2S]$^{2+/+}$ cluster assembly and subsequent delivery to ferredoxins or other enzymes that utilize iron−sulfur clusters to carry out their cellular roles. In this context, it is interesting that when *P. aeruginosa* is challenged with iron-limiting conditions the *bfd* gene is upregulated while that encoding bacterioferritin (*bfr*) is downregulated (*20*). This observation, together with the fact that the *bfd* and *bfr* genes are contiguous, has been used to suggest that the two proteins may interact within the cell and that Bfd may participate in the delivery of iron from or to bacterioferritin (*35*, *40*). Clearly, additional experimentation is needed to test these ideas in the quest to understand the iron assimilation and trafficking events that take place when *P. aeruginosa* is challenged with low iron availability.

In conclusion, the products of two genes upregulated by iron starvation have been characterized and studied. This has led to the surprising observation that the product of the *fpr* gene, a $NADP^+$-dependent ferredoxin reductase, efficiently supports the catalytic activity of *pa*-HO in vitro, without the need for a mediating ferredoxin. The X-ray crystal structure of this enzyme has been determined to 1.6 Å resolution. The fold of *pa*-FPR is almost identical to that of *Av*-FPR, including the bent conformation of the FAD cofactor, which is a distinguishing feature of these two enzymes from the majority of enzymes of known structure in the ferredoxin reductase family. The product of the *bfd* gene, catalogued as bacterioferritin-associated ferredoxin, likely does not function as a classical electron transfer ferredoxin. Rather, it is possible that Bfd functions in the mobilization of iron from bacterioferritin, perhaps as a scaffold for assembling [2Fe-S]$^{2+/+}$ clusters for subsequent transfer to proteins and enzymes that harbor such clusters in their active site.

SUPPORTING INFORMATION AVAILABLE

DNA sequences of *pa*-Bfd and *pa*-FPR engineered with silent mutations to include codons favored by *E. coli*. This material is available free of charge via the Internet at http://pubs.acs.org.

REFERENCES

1. Chipperfield, J. R., and Ratledge, C. (2000) Salicylic Acid is not a Bacterial Siderophore: A theoretical Study, *BioMetals 13*, 165−168.

2. Ward, P. P., and Conneely, O. M. (2004) Lactoferrin: Role in Iron Homeostasis and Host Defense Against Microbial Infection, *BioMetals 17*, 203−208.
3. Flo, T. H., Smith, K. D., Sato, S., Rodriguez, D. J., Holmes, M. A., Strong, R. K., Akira, S., and Aderem, A. (2004) Lipocalin 2 Mediates an Innate Immune Response to Bacterial Infection by Sequestering Iron, *Nature 432*, 917−921.
4. Wandersman, C., and Delepelaire, P. (2004) Bacterial Iron Sources: From Siderophores to Hemophores, *Annu. Rev. Microbiol. 58*, 611−647.
5. Genco, C. A., and Dixon, D. W. (2001) Emerging Strategies in Microbial Haem Capture, *Mol. Microbiol. 39*, 1−11.
6. Otto, B. R., Verweij-van Vught, A. M., and MacLaren, D. M. (1992) Transferrins and Heme-Compounds as Iron Sources of Pathogenic Bacteria, *Crit. Rev. Microbiol. 18*, 217−233.
7. Skaar, E. P., and Schneewind, O. (2004) Iron-regulated surface determinants (Isd) of *Staphylococcus aureus*: Stealing iron from heme, *Microbes Infect. 6*, 390−397.
8. Ochsner, U. A., Johnson, Z., and Vasil, A. I. (2000) Genetics and Regulation of Two Distinct Haem-Uptake Systems, *phu* and *has*, in *Pseudomonas aeruginosa*, *Microbiology 146*, 185−198.
9. Ratliff, M., Zhu, W., Deshmukh, R., Wilks, A., and Stojiljkovic, I. (2001) Homologues of Neisserial Heme Oxygenase in Gram-Negative Bacteria: Degradation of Heme by the Product of the *pigA* Gene of *Pseudomonas aeruginosa*, *J. Bacteriol. 183*, 6394−6403.
10. Yoshida, T., Noguchi, M., and Kikuchi, G. (1980) Oxygenated Form of Heme-Heme Oxygenase Complex and Requirement for Second Electron to Initiate Heme Degradation from the Oxygenated Complex, *J. Biol. Chem. 255*, 4418−4420.
11. Davydov, R. M., Yoshida, T., Ikeda-Saito, M., and Hoffman, B. M. (1999) Hydroperoxy-Heme Oxygenase Generated by Cryoreduction Catalyzes the Formation of α-meso-Hydroxyheme as Detected by EPR and ENDOR, *J. Am. Chem. Soc. 121*, 10656−10657.
12. Wilks, A., Torpey, J., and Ortiz de Montellano, P. R. (1994) Heme Oxygenase (HO-1) Evidence for Electrophilic Oxygen Addition to the Porphyrin Ring in the Formation of α-meso-hydroxyheme, *J. Biol. Chem. 269*, 29553−29556.
13. Yoshida, T., and Kikuchi, G. (1978) Features of the Reaction of Heme Degradation Catalyzed by the Reconstituted Microsomal Heme Oxygenase System, *J. Biol. Chem. 253*, 4230−4236.
14. Yoshida, T., Noguchi, M., and Kikuchi, G. (1980) A New Intermediate of Heme Degradation Catalyzed by the Heme Oxygenase System, *J. Biochem. 88*, 557−563.
15. Liu, Y., and Ortiz de Montellano, P. R. (2000) Reaction Intermediates and Single Turnover Rate Constants for the Oxidation of Heme by Human Heme Oxygenase-1, *J. Biol. Chem. 275*, 5297−5307.
16. Cornejo, J., Willows, R. D., and Beale, S. I. (1998) Phytobilin Biosynthesis: Cloning and Expression of a Gene Encoding Soluble Ferredoxin-Dependent Heme Oxygenase from *Synechocystis* sp. PCC6803, *Plant J. 15*, 99−107.
17. Wegele, R., Tasler, R., Zeng, Y., Rivera, M., and Frankenberg-Dinkel, N. (2004) The Heme Oxygenase(s)-Phytochrome System of *Pseudomonas aeruginosa*, *J. Biol. Chem. 279*, 45791−45802.
18. Cornejo, J., and Beale, S. I. (1997) Phycobilin Biosynthetic Reactions in Extracts of Cyanobacteria, *Photosynth. Res. 51*, 223−230.
19. Muramoto, T., Tsurui, N., Terry, M. J., Yokota, A., and Kohchi, T. (2002) Expression and Biochemical Properties of a Ferredoxin-Dependent Heme Oxygenase Required for Phytochrome Chromophore Synthesis, *Plant Physiol. 130*, 1958−1966.
20. Ochsner, U. A., Wilderman, P. J., Vasil, A. I., and Vasil, M. L. (2002) GeneChip Expression Analysis of the Iron Starvation Response in *Pseudomonas Aeruginosa*: Identification of Novel Pyoverdine Biosynthesis Genes, *Mol. Microbiol. 45*, 1277−1287.
21. Ikemura, T. (1985) Codon Usage and tRNA Content in Unicellular and Multicellular Organisms, *Mol. Biol. Evol. 2*, 13−34.
22. Aliverti, A., Curti, B., Vanoni, M. A. (1999) Identifying and Quantitating FAD and FMN in Simple and in Iron-Sulfur-Containing Flavoproteins, in *Methods in Molecular Biology* (Chapman, S. K., and Reid, G. A., Eds.) Vol. 131, pp 9−23, Humana Press, Totowa, NJ.
23. Macheroux, P. (1999) UV-Visible Spectroscopy as a Tool to Study Flavoproteins, in *Methods in Molecular Biology* (Chapman, S. K., and Reid, G. A., Eds.) Vol. 131, pp 1−7, Humana Press, Totowa, NJ.
24. Deshmukh, R., Zeng, Y., Furci, L. M., Huang, H.-w., Morgan, B. N., Sander, S., Alontaga, A., Bunce, R. A., Moënne-Loccoz, P., Rivera, M., and Wilks, A. (2005) Heme Oxidation in a Chimeric Protein of the α-Selective Neisseriae meningitidis Heme Oxygenase with the Distal Helix of the δ-Selective Pseudomonas aeruginosa, *Biochemistry 44*, 13713−13723.
25. Caignan, G. A., Deshmukh, R., Wilks, A., Zeng, Y., Huang, H., Moënne-Loccoz, P., Bunce, R. A., Eastman, M. A., and Rivera, M. (2002) Oxidation of Heme to β- and δ-biliverdin by *Pseudomonas aeruginosa* Heme Oxygenase as a Consequence of an Unusual Seating of the Heme, *J. Am. Chem. Soc. 124*, 14879−14892.
26. Luft, J. R., Collins, R. J., Fehrman, N. A., Lauricella, A. M., Veatch, C. K., and DeTitta, G. T. (2003) A Deliberate Approach to Screening for Initial Crystallization Conditions of Biological Macromolecules, *J. Struct. Biol. 142*, 170−179.
27. Kabsch, W. (1993) Automatic Processing of Rotation Diffraction Data from Crystals of Initially Unknown Symmetry and Cell Constraints, *J. Appl. Crystallogr. 26*, 795−800.
28. Brunger, A. T., Adams, P. D., Clore, G. M., DeLano, W. L., Gros, P., Grosse-Kunstleve, R. W., Jiang, J. S., Kuszewski, J., Nilges, M., Pannu, N. S., Read, R. J., Rice, L. M., Simonson, T., and Warren, G. L. (1998) Crystallography & NMR System: A New Software Suite for Macromolecular Structure Determination, *Acta Crystallogr. D54*, 905−921.
29. Jones, T. A., and Zhou, J. Y. (1991) Improved Methods for Binding Protein Models in Electron Density Maps and the Location of Errors in These Models, *Acta Crystallogr. A47*, 110−119.
30. Coghlan, V. M., and Vickery, L. E. (1991) Site-Specific Mutations in Human Ferredoxin That Affect Binding to Ferredoxin Reductase and Cytochrome $P450_{SCC}$, *J. Biol. Chem. 266*, 18606−18612.
31. Jacobson, B. L., Chae, Y. K., Böhme, H., Markley, J. L., and Holden, H. M. (1992) Crystallization and Preliminary Analysis of Oxidized, Recombinant, Heterocyst [2Fe-2S] Ferredoxin from *Anabaena* 7120, *Arch. Biochem. Biophys. 294*, 279−281.
32. Palmer, G., Brintzinger, H., and Estabrook, W. (1967) Spectroscopic Studies on Spinach Ferredoxin and Adrenodoxin, *Biochemistry 6*, 1658−1664.
33. Reipa, V., Holden, H. M., Mayhew, M. P., and Vilker, V. L. (2004) Temperature-Induced Structural Changes in Putidaredoxin: A Circular Dichroism and UV-Vis Absorption Study, *Biochim. Biophys. Acta 1699*, 229−234.
34. Golinelli, M. P., Chatelet, C., Duin, E. C., Johnson, M. K., and Meyer, J. (1998) Extensive Ligand Rearrangement Around the [2Fe-2S] Cluster of *Clostridium pasteurianuum* Ferredoxin, *Biochemistry 37*, 10429−10437.
35. Quail, M. A., Jordan, P., Grogan, J. M., Butt, J. N., Lutz, M., Thomson, A. J., Andrews, S. C., and Guest, J. R. (1996) Spectroscopic and Voltammetric Characterization of Bacterioferritin-Associated Ferredoxin of *Escherichia coli*, *Biochem. Biophys. Res. Commun. 229*, 635−642.
36. Fu, W., Jack, R. F., Morgan, T. V., Dean, D. R., and Johnson, M. K. (1994) *nifU* Gene Product from *Azotobacter vinelandii* Is a Homodimer that Contains Two Identical [2Fe-2S] Clusters, *Biochemistry 33*, 13455−13463.
37. Chen, B., Menon, N. K., Dervertarnian, L., Moura, J. J. G., and Przybyla, A. E. (1994) Cloning, Sequencing and Overexpression of the *Desulfovibrio gigas* Ferredoxin Gene in *E. coli*, *FEBS Lett. 351*, 401−404.
38. Fukuyama, K. (2001) Ferredoxins Containing one [4Fe-4S] Center, in *Handbook of Metalloproteins* (Messerschmidt, A., Huber, R., Poulos, T. L., and Wieghardt, K., Eds.) Vol. 1, pp 543−552, John Wiley & Sons, New York.
39. Dailey, H. A., Finnegan, M. G., and Johnson, M. K. (1994) Human Ferrochelatase is an Iron-Sulfur Protein, *Biochemistry 33*, 403−407.
40. Garg, R. P., Vargo, C. J., Cui, X., and Kurtz, D. M., Jr. (1996) A [2Fe-2S] Protein Encoded by an Open Reading Frame Upstream of the *Escherichia coli* Bacterioferritin Gene, *Biochemistry 35*, 6297−6301.
41. Gibson, J. F., Hall, D. O., Thornley, J. H. M., and Whatley, F. R. (1966) Iron Complex in Spinach Ferredoxin, *Proc. Natl. Acad. Sci. U.S.A. 56*, 987−990.
42. Mukai, K., Kimura, T., Helbert, J., and Kevan, L. (1973) Environment of the Iron-Sulfur Chromophore in Adrenodoxin Studied by EPR and ENDOR Spectroscopy, *Biochim. Biophys. Acta 295*, 49−56.
43. Tsibris, J. C. M., Tsai, R. L., Gunsalus, I. C., Orme-Johnson, W. H., Hansen, R. E., and Beinert, H. (1968) The Number of Iron Atoms in the Paramagnetic Center (G = 1.94) of Reduced

Putidaredoxin, a Nonheme Iron Protein, *Proc. Natl. Acad. Sci. U.S.A. 59*, 959−965.
44. Ozaki, Y., Nagayama, K., Kyogoku, Y., Hase, T., and Matsubara, H. (1983) Resonance Raman Spectroscopic Study on the Iron-Sulfur Proteins Containing [2Fe-2S] Clusters, *FEBS Lett. 152*, 236−240.
45. Johnson, M. K., Hare, J. W., Spiro, T. G., Moura, J. J. G., Xavier, A. V., and LeGall, J. (1981) Resonance Raman Spectra of Three-Iron Centers in Ferredoxins from *Desulfovibrio gigas*, *J. Biol. Chem. 256*, 9806−9808.
46. Johnson, M. K., Spiro, T. G., and Mortensen, L. E. (1982) Resonance Raman and Electron Paramagnetic Resonance Studies on Oxidized and Ferricyanide-Treated *Clostridium pasteurianum* Ferredoxin, *J. Biol. Chem. 257*, 2447−2452.
47. Moulis, J. M., Lutz, M., Gaillard, J., and Noodleman, L. (1988) Characterization of $[4Fe\text{-}4Se]^{2+/3+}$ High-Potential Iron-Sulfur Protein from *Chromatium vinosum*, *Biochemistry 27*, 8712−8719.
48. Fu, W., Drozdzewski, P. M., Davies, M. D., Sligar, S. G., and Johnson, M. K. (1992) Resonance Raman and Magnetic Circular Dichroism Studies of Reduced [2Fe-2S] Proteins, *J. Biol. Chem. 267*, 15502−15510.
49. Meyer, J., Fujinaga, J., Gaillard, J., and Lutz, M. (1994) Mutated Forms of the [2Fe-2S] Ferredoxin form *Clostridium pasterurianum* with Noncysteinyl Ligands to the Iron-Sulfur Cluster, *Biochemistry 33*, 13642−13650.
50. Han, S., Czernuszewicz, R. S., Kimura, T., Adams, M. W. W., and Spiro, T. G. (1989) Fe_2S_2 Protein Resonance Raman Spectra Revisited: Structural Variations among Adrenodoxin, Ferredoxin, and Red Paramagnetic Protein, *J. Am. Chem. Soc. 111*, 3505−3511.
51. Han, S., Czernuszewicz, R. S., and Spiro, T. G. (1989) Vibrational Spectra and Normal Mode Analysis for [2Fe-2S] Protein Analogues Using ^{34}S, ^{54}Fe, and ^{2}H Substitution: Coupling of Fe-S Stretching and S-C-C Bending Modes, *J. Am. Chem. Soc. 111*, 3496−3504.
52. Higashimoto, Y., Sato, H., Sakamoto, H., Takahashi, K., Palmer, G., and Noguchi, M. (2006) The Reactions of Heme- and Verdoheme-Heme Oxygenase-1 Complexes with FMN-depleted NADPH-Cytochrome P450 Reductase, *J. Biol. Chem. 281*, 31659−31667.
53. Damaso, C. O., Bunce, R. A., Barybin, M. V., Wilks, A., and Rivera, M. (2005) The Ferrous Verdoheme-Heme Oxygenase Complex is Six-Coordinate and Low-Spin, *J. Am. Chem. Soc. 127*, 17852−17853.
54. Lipscomb, J. D., Sligar, S. G., Namtvedt, M. J., and Gunsalus, I. C. (1976) Autooxidation and Hydroxylation Reactions of Oxygenated Cytochrome $P\text{-}450_{cam}$, *J. Biol. Chem. 251*, 1116−1124.
55. Ortiz de Montellano, P. R., and Wilks, A. (2000) Heme Oxygenase Structure and Mechanism, *Adv. Inorg. Chem. 51*, 359−407.
56. Rivera, M., and Zeng, Y. (2005) Heme oxygeanse, Steering Dioxygen Activation Toward Heme Hydroxylation, *J. Inorg. Biochem. 99*, 337−354.
57. Higashimoto, Y., Sakamato, H., Hayashi, S., Sugishima, M., Fukuyama, K., Palmer, A. G., and Noguchi, M. (2005) Involvement of NADP(H) in the Interaction between Heme Oxygenase-1 and Cytochrome P450 Reductase, *J. Biol. Chem. 280*, 729−737.
58. Prasad, G. S., Kresge, N., Muhlberg, A. B., Shaw, A., Jung, Y. S., Burgess, B. K., and Stout, C. D. (1998) The Crystal Structure of NADPH:Ferredoxin Reductase from *Azotobacter vinelandii*, *Protein Sci. 7*, 2541−2549.
59. Ingelman, M., Bianchi, V., and Eklund, H. (1997) The Three-Dimensional Structure of Flavodoxin Reductase from *Escherichia coli* at 1.7 ×81 Resolution, *J. Mol. Biol. 268*, 147−157.
60. Karplus, P. A., Daniels, M. J., and Herriott, D. J. R. (1991) Atomic Structure of Ferredoxin-$NADP^+$ Reductase: Prototype for a Structurally Novel Flavoenzyme Family, *Science 251*, 60−66.
61. Carrillo, N., and Ceccarelli, E. A. (2003) Open Questions in Ferredoxin-$NADP^+$ Reductase Catalytic Mechanism, *Eur. J. Biochem. 270*, 1900−1915.
62. Avila, L., Huang, H.-w., Rodríguez, J. C., Moënne-Loccoz, P., and Rivera, M. (2000) Oxygen Activation by Axial Ligand Mutants of Mitochondrial Cytochrome b_5: Oxidation of Heme to Verdoheme and Biliverdin, *J. Am. Chem. Soc. 122*, 7618−7619.
63. Sigman, J. A., Wang, X., and Lu, Y. (2001) Coupled Oxidation of Heme by Myoglobin is Mediated by Exogenous Peroxide, *J. Am. Chem. Soc. 123*, 6945−6946.
64. Avila, L., Huang, H., Damaso, C. O., Lu, S., Moënne-Loccoz, P., and Rivera, M. (2003) Coupled Oxidation vs Heme Oxygenation: Insights from Axial Ligand Mutants of Mitochondrial Cytochrome b_5, *J. Am. Chem. Soc. 125*, 4103−4110.
65. Friedman, J., Lad, L., Li, H., Wilks, A., and Poulos, T. L. (2004) Structural Basis for Novel δ-Regioselective Heme Oxygenation in the Opportunistic Pathogen *Pseudomonas aeruginosa*, *Biochemistry 43*, 5239−5245.
66. Rodriguez, J. C., Wilks, A., and Rivera, M. (2006) Backbone NMR Assignments and H/D Exchange Studies on the Ferric Azide- and Cyanide-Inhibited Forms of *Pseudomonas aeruginosa* Heme Oxygenase, *Biochemistry 45*, 4578−4592.
67. Zuiderweg, E. R. P. (2002) Mapping Protein-Protein Interactions in Solution by NMR Spectroscopy, *Biochemistry 41*, 1−7.
68. Bianchi, V., Haggard-Ljungquist, E., Pontis, E., and Reichard, P. (1995) Interruption of the Ferredoxin (Flavodoxin) $NADP^+$ Oxidureductase Gene in *Escherichia coli* Does Not Affect Anaerobic Growth but Increases Sensitivity to Paraquat, *J. Bacteriol. 177*, 4528−4531.
69. Krapp, A. R., Rodriguez, R. E., Poli, H. O., Paladini, D. H., Platnik, J. F., and Carrillo, N. (2002) The Flavoenzyme Ferredoxin (Flavodoxin)-NADP(H) Reductase Modulates NADP(H) Homeostasis During the *soxRS* Response in *Escherichia coli*, *J. Bacteriol. 184*, 1474−1480.
70. Isas, J. M., and Burgess, B. K. (1994) Purification and Characterization of $NADP^+$/NADPH-Specific Flavoprotein That is Overexpressed in FdI^- Strains of *Azotobacter vinelandii*, *J. Biol. Chem. 269*, 19404−19409.
71. Bianchi, V., Reichard, P., Eliasson, R., Pontis, E., Krook, M., Jornvall, H., and Haggard-Ljungquist, E. (1993) *Escherichia coli* Ferredoxin $NADP^+$ Reductase: Activation of *E. coli* Anaerobic Ribonucleotide Reduction, Cloning of the Gene (*fpr*), and Overexpression of the Protein, *J. Bacteriol. 175*, 1590−1595.
72. Razquin, P., Fillat, M. F., Schmitz, S., Bohme, H., Gomez-Moreno, C., and Peleato, M. L. (1996) Expression of Ferredoxin-$NADP^+$ Reductase in Hetocysts from *Anabaena* sp., *Biochem. J. 316*, 157−160.
73. Dos Santos, P. C., Smith, A. D., Frazzon, J., Cash, V. L., Johnson, M. K., and Dean, D. R. (2004) Iron-Sulfur Cluster Assembly: NifU-Directed Activation of the Nitrogenase Fe Protein, *J. Biol. Chem. 279*, 19705−19711.

BI7013135